Design and Fabrication of an Optimized Cylindrical Electromagnetic Pulsed Actuator

Juan Manuel Rosselló[1,2,3], Fabián Eduardo Giana[1,2,3], and Fabián José Bonetto[1,2,3]

[1]Consejo Nacional de Investigaciones Científicas y Técnicas, Buenos Aires C1425FQB, Argentina
[2]Laboratorio de Cavitación y Biotecnología, Centro Atómico Bariloche, CNEA, Bariloche 8400, Argentina
[3]Instituto Balseiro, Universidad Nacional de Cuyo, Mendoza M5502JMA, Argentina

In this paper, we present a strategy for designing a high-power linear electromagnetic pulsed actuator considering thermal, electromagnetic, and mechanical aspects. The optimization process was based on a first-principle calculation of the maximum current that the different parts of the coil and the materials conforming the device can resist without taking damage or altering their properties significantly due to thermal or mechanical stresses. Specifically, the minimum coil resistance (and the maximum safe current) for a given applied voltage was computed for a variety of wire diameters. Then, we employed a tailored numerical code to compute the coil geometry that produces the maximum pull/push force per ampere for typical commercial permanent magnet sizes. The combination of the optimized coil resistance and the optimized normalized force gives a maximized total force developed in the solenoid actuator. The designed coil was fabricated and characterized in order to analyze its performance. The results were compared with the calculations to perform an experimental validation of the numerical code obtaining and excellent agreement between computed and experimental results.

Index Terms— **Optimized geometry, permanent magnet, pulsed magnetic actuator.**

I. Introduction

An electromagnetic actuator is an electromechanical device designed to transform electrical current in mechanical work. Linear actuators can be rather useful in industrial and scientific applications (such as valve actuation, pin-puller, precision positioners, magnetic bearings, and so on) because they can be easily controlled and have short response times (compared to compressed air or hydraulic systems), but also due to their absence of mechanical parts which implies a reduced friction and low maintenance costs. The appearance of strong hard permanent magnets (like NdFeB or AlNiCo) allowed the design of efficient high-precision actuators with the advantage of having a passive nucleus [2]. This kind of device can be operated with a low-power continuous alternating signal [3] or driven with high-power pulses [4]. The main limitation of high-power actuators is the overheating of the coils that generate the magnetic field, affecting not only their duty cycle but also their performance stability.

Recently, analytical approaches for modeling the magnetic interaction between a thin cylindrical coil and a permanent magnet with axial polarization have been published [5]–[7]. Furthermore, Robertson *et al.* [1] compared a variety of analytical/integral methods and developed a numerical code [available for public use in the website (http://github.com/wspr/magcode)] for designing a "sleeve-type" actuator with optimized geometry.

In this paper, we present a strategy for designing a linear electromagnetic pulsed actuator considering thermal, electromagnetic, and mechanical aspects. Specifically, we have based the whole optimization process on a first-principle calculation of the maximum current that the coil (i.e., the winding, the magnets, and the bobbin) and the materials conforming the device can hold out without taking damage or altering their properties. Moreover, the minimum coil resistance for a given applied voltage was set for a variety of wire diameters. Then, we employed Robertson's code to compute the coil geometry that produces the maximum pull/push force per ampere for typical commercial permanent magnet sizes. The combination of the optimized coil resistance and the optimized normalized force gives a maximized total force developed in the solenoid actuator [1]. Furthermore, the coil bobbin design was also optimized by minimizing the distance between the coil and the permanent magnet but still making the bobbin thick enough to withstand the tensions involved.

The designed coil was fabricated following the specific requirements of the experimental device described in [8] and [9] and characterized in order to analyze its performance. The results were compared with the numerical calculations to perform an experimental validation of Robertson's code.

Manuscript received March 16, 2018; accepted June 22, 2018. Corresponding author: J. M. Rosselló (e-mail: jrossello@cab.cnea.gov.ar).

Color versions of one or more of the figures in this paper are available online at http://ieeexplore.ieee.org.

Digital Object Identifier 10.1109/TMAG.2018.2850802

II. Actuator Design

A. Coil Heating in Pulsed Operation

When designing a device driven by high currents, one of the critical aspects is the heat generation within its components. Particularly, in a pulse-operated actuator, the coil is energized for very short time intervals; therefore, the heat transfer is sufficiently fast to suppose an adiabatic process. The maximum duration and intensity of a safe current pulse are thus determined by the initial and final temperatures of the coil and, naturally, by the characteristics of its material.

During the time interval Δt at which the actuator is energized, the coil metal is uniformly heated by the Joule effect, increasing its temperature from T_i (293 K in this paper) to T_f.

Considering a uniform current density within the metal, then the ohmic heating can be written as

$$\rho_{\mathrm{el}}(T)[j(t)]^2 dt = \rho c(T) dT \tag{1}$$

where $j(t)$ represents the current density, ρ is the mass density of the metal, $c(T)$ is its heat capacity, and $\rho_{\mathrm{el}}(T)$ is its electrical resistivity. For a current pulse with a duration t_p, the final temperature T_f can be obtained by numerically integrating (1)

$$\int_0^{t_p} [j(t)]^2 dt = \int_{T_i}^{T_f} \frac{\rho c(T)}{\rho_{\mathrm{el}}(T)} dT. \tag{2}$$

The integral on the left side of (2) can be rewritten as [4]

$$\int_0^{t_p} [j(t)]^2 dt = j_0^2 t_p \xi \tag{3}$$

where j_0 is the amplitude of $j(t)$ and ξ is a form factor of the current pulse whose values are $\xi = 1$ for a rectangular pulse, $\xi = 1/2$ for the semi-period of a sinusoidal waveform, and $\xi = 1/3$ for a triangle pulse. In order to compute the integral on the right side of (2), it is necessary to know how ρ_{el} and c vary with temperature. At temperatures higher than 100 K, the electrical resistivity can be approximated by [10]

$$\rho_{\mathrm{el}}(T) = \rho_{\mathrm{el}}(T_i)[1 + \beta_T (T - T_i)] \tag{4}$$

where β_T is the temperature coefficient of resistance of the winding material. For copper at temperatures higher than 200 K, β_T takes values given by [11]

$$\beta_T^{\mathrm{Cu}} = \frac{1}{[233.54 + (T - 273.15)]}. \tag{5}$$

On the other hand, the dependence of the heat capacity $c(T)$ with temperature is given by Debye model [12]

$$c(T) = 9 n k_B \frac{\theta_D}{T} \int_0^{\frac{\theta_D}{T}} \frac{x^4 e^x}{(e^x - 1)^2} dx \tag{6}$$

where n is the molar density, while k_B and θ_D represent Boltzmann's constant and the Debye temperature, respectively. θ_D is an empirical parameter whose value is 315 K for copper.

Based on equations (3)–(6), a numerical solution of the integral in (2) was found for a copper wire ($\rho = 8.89 \times 10^3$ kg/m^3, $\rho_{\mathrm{el}}(293\ K) = 1.71 \times 10^{-8}$ Ωm) assuming a rectangular current pulse.

Considering the fact that the insulating varnish of a typical annealed copper wire deteriorates at temperatures higher than 425 K (152 °C), the temperature range for computing the integral was chosen between $T_i = 293$ K and $T_f = 425$ K, and the maximum current intensity that could be circulated through the wire ($I_C^{\max}$) was then computed as a function of the wire diameter d_w and pulse duration t_p. The results of the latter are shown in Fig. 1(a) together with some empirical reference values corresponding to direct current [13]. Changes in the coil resistance due to magnetoresistance effect are insignificant in the range of temperatures and magnetic field strengths considered in [4].

The previous computation was carried out by assuming an adiabatic and homogeneous heating. These hypotheses imply that the effect of heat loss by means of convection and

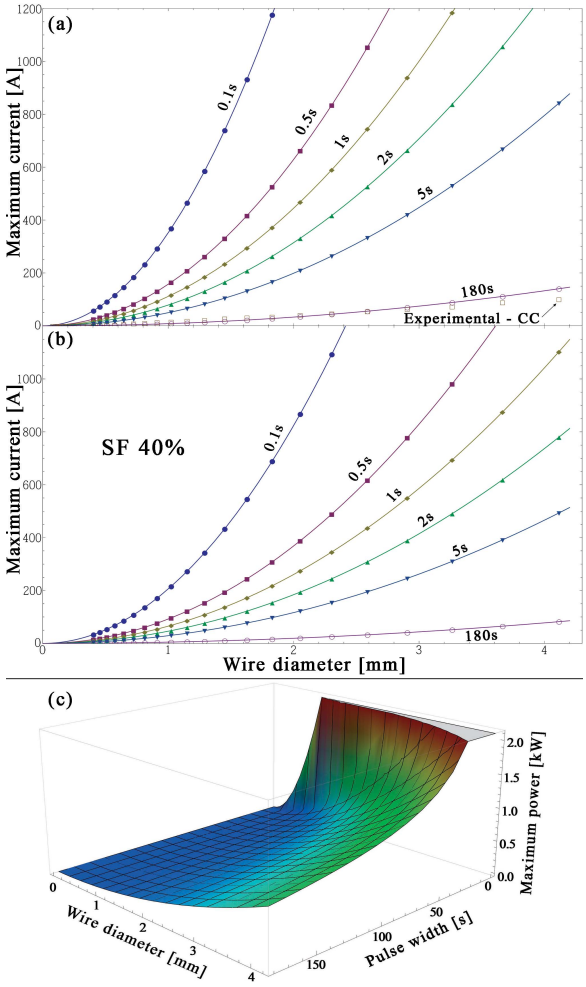

Fig. 1. Maximum current pulse amplitude computed for a standard annealed copper wire as a function of the wire diameter (d_w) and the pulse duration (t_p). (a) Maximum admissible temperature was set in 425 K, considering that the wire electric insulation begins to deteriorate at that temperature. Empirical values for continuous current were also included. (b) In these calculations, SF40% was used taking into account the thermal response of typical NdFeB magnets and also to avoid an overheating of the bobbin material. (c) Maximum power surface as a function of d_w and t_p for the case with SF40%.

radiation processes in the coil must be far less than the effect of Joule heating. The heating homogeneity (i.e., the absence of thermal gradients within the coil) was checked by computing the Biot number $\mathrm{Bi} = L_C h/k$ [14]. $\mathrm{Bi} \ll 1$ indicates a uniform temperature in the solid and a low rate of heat transfer toward its exterior. Considering a convection coefficient of $h = 20$ W/(m^{2}K), a thermal conductivity of $k = 375$ Wm/K [14], and a coil thickness $L \leq 50$ mm, we have a $\mathrm{Bi} \leq 0.002$. The relationship between the electrical power applied to the coil P_{elec} and the power dissipated by convection and radiation mechanisms was also computed, employing the limit current values presented in Fig. 1(a) and a typical coil with length $l_C = 40$ mm, external radius $R_C = 40$ mm, and internal radius $r_C = 10$ mm. The power dissipated by convection for the stationary case is calculated as

$$P_{\mathrm{conv}} = A_s h (T - T_\infty) \tag{7}$$

where A_s is the coil surface area and T_∞ is the room temperature. On the other hand, the power dissipated by radiation is

given by Stefan–Boltzmann law [14]

$$P_{\text{rad}} = A_s \varepsilon \sigma_{\text{SB}} \left(T^4 - T_\infty^4\right) \tag{8}$$

where σ_{SB} is Stefan–Boltzmann's constant and ε the thermal emissivity coefficient ($\varepsilon \approx 0.045$ for copper at $T \approx 373$ K). Assuming an average temperature of 80 °C and $T_\infty = 20$ °C in the coil, (7) and (8) give $P_{\text{rad}} \approx 0.5$ W and $P_{\text{conv}} \approx 28$ W. The resulting power ratio $(P_{\text{conv}} + P_{\text{rad}})/P_{\text{elec}}$ takes values between 10^{-3} and 10^{-2} for wire diameters ranging from 4 to 1 mm, respectively. Then, considering that $(P_{\text{conv}} + P_{\text{rad}})/P_{\text{elec}} \ll 1$, it is safe to assume an adiabatic behavior of the coil heating under these operating conditions.

To complete this analysis, we must consider the thermal properties of the remaining materials conforming the magnetic actuator, in particular, the coil bobbin and the permanent magnets. As detailed in Section III-A, the coil bobbin employed in this paper was made from polyamide 6, whose "glass temperature" (i.e., the temperature at which the stiffness is significantly reduced) is approximately 55 °C [20]. Regarding to the coil nucleus, we must consider that it can absorb some of the heat during successive executions of the actuator. Thus, the strength of the permanent magnet in the nucleus can change as its temperature is raised, affecting the performance stability of the device. For a typical NdFeB magnet, the remanence and the coercivity decay 4% and 24%, respectively, for temperatures between 20 °C and 55 °C [19]. If the coil is energized by a voltage source instead of a current source, an increase in the coil resistance of 10% should also be considered for the same temperature range. Taking into account these constraints and other minor thermal effects not included in the previous calculations, the optimization process described in Section III was performed by computing the maximum currents for a limiting wire temperature of 55 °C (328 K), which is equivalent to taking a safety factor of 40% (SF40%). It is worth noting that the safety factor was taken on the maximum temperature and not on the computed applied current, since the model in (1) is not linear with temperature. This is particularly important when the actuator application requires some stability criteria. The results computed for this case are shown in Fig. 1(b). In addition, Fig. 1(c) presents the maximum power applied to the coil using the SF40% criteria as a function of the wire diameter and the pulse duration.

B. Geometrical Optimization

When designing a coil one must define which parameters are system variables and which ones are fixed values, depending on the specific application and the available experimental capabilities. There are many different parameters to establish the optimization criteria, for example, the coil power consumption, the maximum stroke length, the maximum force ($|\vec{F}_C|$), the maximum force per ampere ($|\vec{f}_C|$), the response time, or the performance stability.

In this section, we use numerical simulations to find the design parameters of the actuator that maximize the axial force between a thick cylindrical coil and a cylindrical permanent magnet [1]. For this purpose, it is necessary to maximize the amplitude of the magnetic field generated by the coil $|\vec{B}_C|$

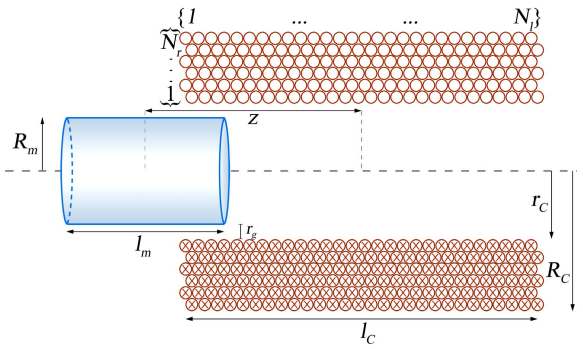

Fig. 2. Schematic of a "sleeve coil" magnetic actuator of cylindrical geometry. The main parameters used in its design and optimization are detailed. The coil nucleus is formed from a permanent magnet.

and simultaneously adjust the coil geometry to achieve an optimum interaction between the magnet and $|\vec{B}_C|$, then the maximum (safe) driving current ($I_C^{\max}$) [shown in Fig. 1(b)] must be applied. In pulsed operation actuators, high current amplitudes are commonly produced using a voltage source rather than a current source, mainly because of the high costs and low response times of the latter. Then, the driving voltage (ΔV_C) must be fixed, which in turn limits the coil resistance to a minimum $R_{\text{Coil}}^{\min} = \Delta V_C / I_C^{\max}$.

The optimization process of the actuator geometry was carried out by the following analysis presented by Robertson *et al.* [1]. The magnet remanence (B_r) was supposed to be homogeneous in the axial direction and its coercivity sufficiently is high so as to avoid significant changes in its magnetization due to magnetic induction produced by the external field. A schematic of the system including the geometrical parameters involved in the optimization process is presented in Fig. 2. In particular, we analyzed the magnet aspect ratio $\alpha = l_m/R_m$ (i.e., the ratio between length and radius), the coil aspect ratio $\beta = l_C/r_C$, the radial spacing between the magnet and the coil $r_g = r_C - R_m$, and the distance between their geometrical centers z (which we will call "displacement"). The optimal displacement of the nucleus ($z = z_{\text{op}}$) represents the relative position of the magnet which produces an absolute maximum of the interaction force.

First, the geometrical parameters α and β were studied for two prototypical cases with $I_C = 1$ A, $\Delta V_C = 10$ V, wire diameters of $d_w = 1$ mm (18 AWG) and $d_w = 2.59$ mm (10 AWG), and a resistance equal to the minimum calculated by $R_{\text{Coil}}^{\min} = 10V/I_C^{\max}$ for each wire diameter and a pulse duration of 1 s. Considering that the magnet ratio might not be completely arbitrary, the values of α employed in the computations were adjusted according to different geometries of NdFeB permanent magnets available in the local market. The value of B_r was provided by the magnet supplier (Artic S.A.) being (1.02±0.01) T for the model ARTIC35. Fig. 3 shows the maximum force per ampère ($|\vec{f}_C^{\max}|$) computed for different values of α considering a gap $r_g = 4$ mm between the magnet and the coil. For each value of α, the coil aspect ratio β was varied until reaching an optimal value (i.e., the value of β that maximizes the force).

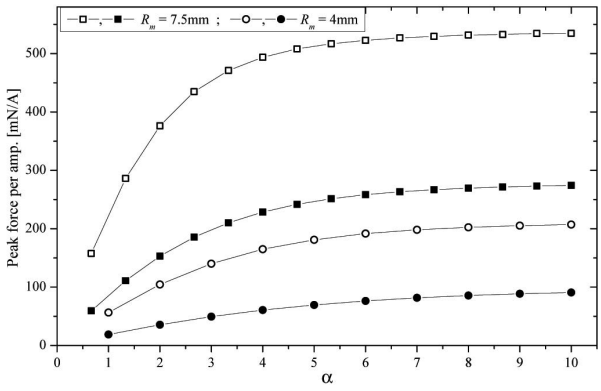

Fig. 3. Simulation of the peak force per ampere developed by the actuator as a function of the geometrical ratio α found in different commercial magnets with $B_r = 1.02$ T. For each value of α, β was varied between 0.1 and 10 and the value producing the maximum force was taken. The calculation was performed for a prototypical case with $\Delta V_C = 10$ V and the minimum resistance $R_{\text{Coil}}^{\min} = \Delta V_C / I_C^{\max}$ computed for two wire diameters. Solid markers: cases with 10 AWG wire. Empty markers: cases with 18 AWG wire. The observed system behavior is similar for other wire diameters.

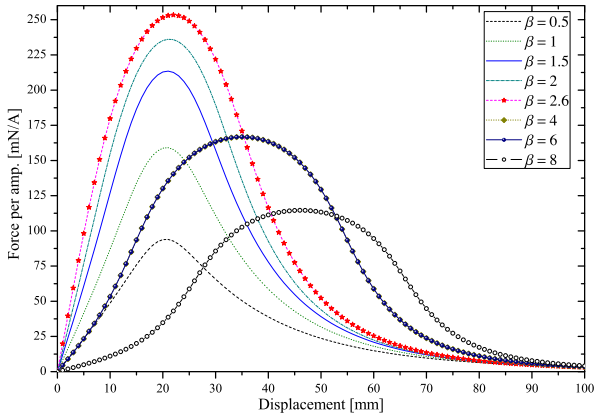

Fig. 4. Simulation of the force per ampere exerted by the actuator as a function of the magnet displacement (z), for different values of the coil aspect ratio β and a fixed magnet aspect ratio $\alpha = 5.33$. The calculation was made for a prototypical case with a 10 AWG wire ($d_w = 2.59$ mm), a magnet with $B_r = 1.02$ T and a radius $R_m = 7.5$ mm, and $\Delta V_C = 10$ V. The optimum value for β varies for different d_w.

The curves shown in Fig. 3 indicate that the higher the magnet volume, the higher its interaction force with the field generated in the coil ($\vec{B}_C$) for a fixed applied current. Moreover, this increment approaches a limit value as l_C increases sufficiently to make the influence of $\vec{B}_C$ over one of the magnet end negligible. Taking these results into account, we decided to employ a magnet with $R_m = 7.5$ mm, $l_m = 40$ mm, and $\alpha = 5.33$. It is worth mentioning that the observed system behavior is similar for other wire diameters.

Once a fixed value for α has been chosen, simulations of $|\vec{f}_C|$ as a function of the displacement z were carried out for different values of β in order to find the optimal coil aspect ratio. Fig. 4 shows an example of the results obtained for a wire diameter of 10 AWG ($d_w = 2.59$ mm). Similar to the analysis shown in Fig. 3, the calculations included in Fig. 4 were performed using the values of $R_{\text{Coil}}^{\min}$ and $I_C^{\max}$ obtained in Section II-A for $d_w = 2.59$ mm. For each value of β, the normalized force reaches a defined local maximum. In Fig. 4, the highest peak force is reached for

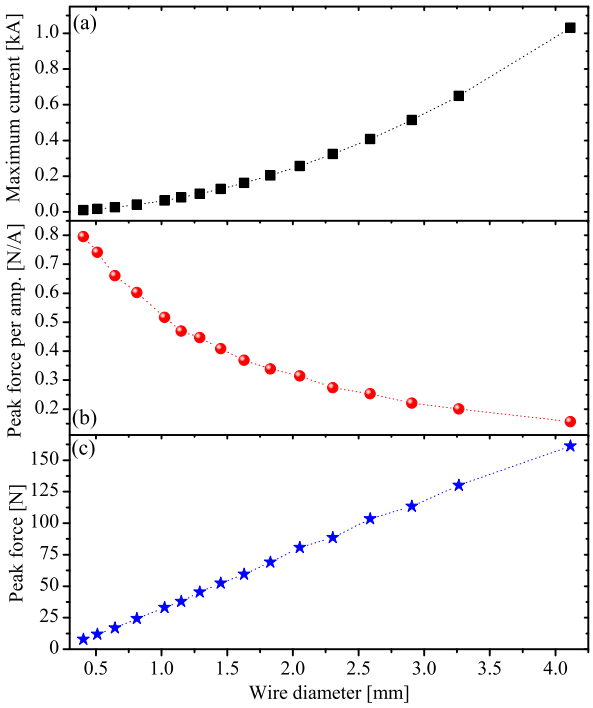

Fig. 5. Computed maximum performance values of an actuator with geometrical ratios $\alpha = 5.33$ as a function of d_w. In each case, $\beta = \beta_{\text{op}}$. In this simulation, the applied voltage was set at $\Delta V_C = 10$ V, and the resistance R_{Coil} was the minimum possible producing the values of $I_C^{\max}$ shown in Fig. 1(b) for $t_p = 1$ s. The remanence of the magnets was $B_r = 1.02$ T. (a) Maximum allowable winding current. (b) Peak force per ampere exerted by the actuator. As d_w is increased, the number of turns composing the coil is reduced and also the maximum force per ampere is generated. (c) Total peak force developed by the actuator $|\vec{F}_C|$.

the optimal values $\beta_{\text{op}} \approx 2.6$ and $z_{\text{op}} = 22$ mm. However, the optimal value of β can be chosen depending on the particular application of the device. For example, if a variation of $|\vec{f}_C|$ smaller than 10% is needed, the maximum stroke would be reduced to a given interval for each β to satisfy the stability requirement of $|\vec{f}_C|$ with z (e.g., the maximum stroke would be ~12 mm for $\beta = 2.6$ and more than 30 mm for $\beta = 8$). It is important to clarify that the optimal value of β_{op} varies for different wire diameters and values of α.

C. Electrodynamical Analysis

After having adjusted the geometric parameters of the system using the results obtained from the thermal analysis, it still remains to prove that the values of $R_{\text{Coil}}^{\min}$ and $I_C^{\max}$ given in Section II-A actually maximize the total peak force ($|\vec{F}_C|$) generated by the actuator. The existence of an optimal wire diameter for the coil is also investigated.

The total peak force is defined as the product between the maximum admissible current and the maximum force per ampère [1]

$$|\vec{F}_C| = \left|\vec{F}_C\left(\alpha, \beta, I_C^{\max}, R_{\text{Coil}}^{\min}, d_w\right)\right| = I_C^{\max}\left|\vec{f}_C^{\max}\right|. \quad (9)$$

Fig. 5 shows the simulated results for the maximum current, the peak force per ampère, and the total peak force as a function of the wire diameter, for an applied voltage of

$\Delta V_C = 10$ V and the minimum coil resistance $R_{\text{Coil}}^{\min}$ (giving $I = I_C^{\max}$). The excitation signal was defined as a rectangular current pulse with $t_p = 1$ s.

Fig. 5(a) shows that for a fixed voltage applied to the inductor, an increase in the diameter of the wire leads to a lower resistance per unit length, whereby the maximum allowable current $I_C^{\max}$ increases rapidly. In these simulations, the total wire length (l_w) is the same regardless of d_w. This arises from the fact that on one hand

$$l_w = \frac{R_{\text{Coil}}^{\min} \frac{\pi}{4} (d_w)^2}{\rho_{\text{el}}} \tag{10}$$

and on the other hand

$$I_C^{\max} = j_{0\max} \frac{\pi}{4} (d_w)^2 = \frac{\Delta V_C}{R_{\text{Coil}}^{\min}} \tag{11}$$

resulting in

$$l_w = \frac{\Delta V_C}{(j_{0\max} \rho_{\text{el}})}. \tag{12}$$

This implies that as d_w is increased, the number of turns constituting the inductor is reduced, decreasing $|\vec{B}_C|$ and consequently the maximum force per ampere [see Fig. 5(b)]. Despite this reduction in $|\vec{f}_C^{\max}|$, Fig. 5(c) shows that the total peak force developed by the actuator $|\vec{F}_C|$ would be greater for large wire diameters. It is important to note that in a real application, the amplitude of current that can be delivered to the inductor will be limited by the battery or the particular voltage/current source used; therefore, there is an optimal value of d_w for which I_C and $|\vec{F}_C|$ are maximized.

To complete the design stage, it remains to verify if $R_{\text{Coil}}^{\min}$ (determined by a purely thermodynamic condition) does in fact maximize $|\vec{F}_C|$. That is, given fixed values of d_w and ΔV_C it should be verified that an increase in R_{Coil}, and the use of a current less than $I_C^{\max}$, do not produce a value of $|\vec{F}_C|$ greater than the one calculated in Fig. 5(c). For this purpose, simulations of the interaction between the permanent magnet and the optimal winding were carried out, changing its resistance between 100 mΩ and 6 Ω for two different wire diameters (10 and 18 AWG). The results are shown in Fig. 6.

In Fig. 6(a), it can be seen how an increase in R_{Coil} limits the current according to $I_C = (\Delta V_C / R_{\text{Coil}})$, while $|\vec{f}_C^{\max}|$ increases considerably as l_w and the number of turns (N) increase along with R_{Coil} [Fig. 6(b)]. However, the total peak force exerted by the actuator $|\vec{F}_C|$ is clearly superior for the cases with low resistance and high current as shown in Fig. 6(c), so that the values of $R_{\text{Coil}}^{\min}$ and $I_C^{\max}$ are indeed optimal for this system. It is important to note that in spite of the higher efficiency of the actuators with high coil resistance (i.e., higher values of $|\vec{f}_C^{\max}|$), the potentially huge wire lengths and bobbin dimensions were not considered in this analysis and should be taken into account to achieve a "realistic" design of the device.

D. Time Constant of the Coil

Having determined the optimum coil parameters configuration ($\alpha, \beta, R_{\text{Coil}}^{\min}, and I_C^{\max}$), it was possible to estimate a theoretical value for its inductance L_{Coil} through Wheeler

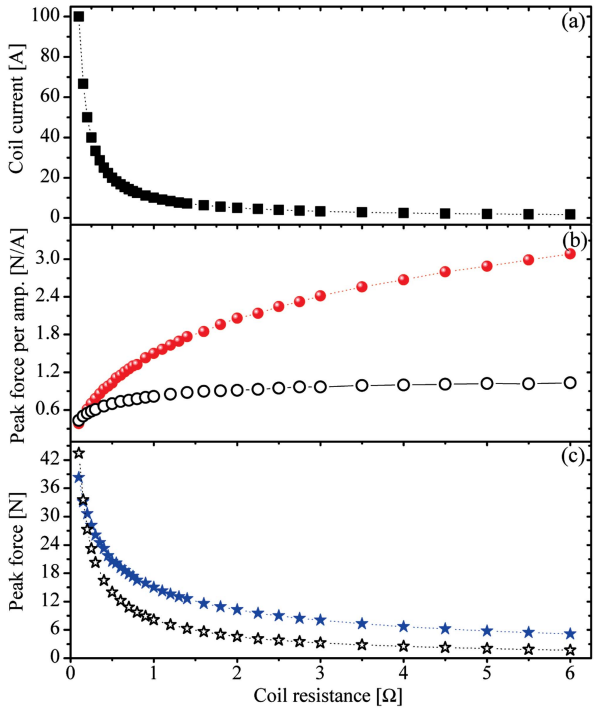

Fig. 6. Simulated maximum performance values as a function of the electric resistance of the coil winding R_{Coil}. The applied voltage was set to $\Delta V_C = 10$ V, and the geometrical ratios were $\alpha = 5.33$ and β was the optimum for each value or R_{Coil}. The remanence of the magnets was $B_r = 1.02$ T. Hollow markers: wire diameter of $d_w = 2.58$ mm (10 AWG). Solid markers: correspond to $d_w = 1$ mm (18 AWG). (a) Maximum allowable winding current. (b) Force per ampere exerted by the actuator. (c) Total peak force developed by the actuator $|\vec{F}_C|$. The force is maximum when the R_{Coil} matches the minimum value computed with the thermal analysis (i.e., $R_{\text{Coil}} = \Delta V_C / I_C^{\max}$).

formula [15]. If distances are used in units of centimeter, the formula can be written as

$$L_{\text{Coil}} = \frac{(R_C + r_C)^2 N^2}{114 l_C + 165 R_C + 89 r_C} \quad [\mu\text{H}]. \tag{13}$$

The values of L_{Coil} and $R_{\text{Coil}}^{\min}$ can be used to calculate the time constant of the coil $\tau_{\text{Coil}} = (L_{\text{Coil}} / R_{\text{Coil}}^{\min})$ and the rise time $T_r = \ln(9) \tau_{\text{Coil}}$. These parameters allow to verify if the response time of the system (without considering inertial effects) satisfies the design requirements of the actuator, and also if the voltage step (that was assumed ideal) fulfills the condition $T_r \ll t_p$.

The present design can be operated in a pulsed fashion with a single pulse or a burst of multiple pulses with a positive or alternating sign. In the latter case, it must be taken into account that the total power delivered must not exceed the one calculated by means of (3), and that its frequency should not exceed the upper cutoff frequency (or in this case the bandwidth) of the system defined as $f_{\text{HC}} = (1/2\pi\, \tau_{\text{Coil}})$. Here, we are considering that any potential inductive effects of the moving magnet can be neglected. This is valid when a reduced stroke configuration is used and/or the magnet displacement velocity is not enough to produce a significantly induced voltage on the coil. Fig. 7 presents the rise time T_r and the frequency f_{HC} calculated for the windings of Fig. 5.

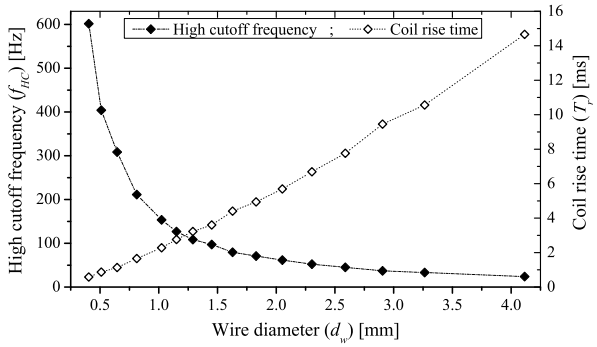

Fig. 7. High cutoff frequency (f_{HC}) and rise time (T_r) for different coils as a function of their wire diameter. The data for each d_w were computed using the optimized geometrical parameters (R_C, r_C, and l_C) in 13.

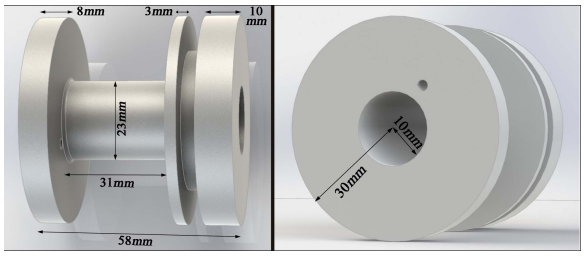

Fig. 8. CAD representation of the coil bobbin with its dimensions. The fabricated piece was made from polyamide 6.

In this paper, we chose to use a 10 AWG wire ($d_w = 2.59$ mm) because its diameter meets the requirements of $I_C^{\max}$ and $|\vec{F}_C|$ of the specific application (described in [8] and [9]) for which the prototype described in Section III was designed. The main parameters of the prototype are detailed in Table I. The outer radius R_C was calculated as $R_C = ((l_w d_w^2/\pi\, l_C) + r_C^2)^{1/2}$ [1]. In particular, the estimated response time for the experimental coil was $T_r^{10\ \mathrm{AWG}} = 7.73$ ms $\ll t_p = 1$ s and its high cutoff frequency is $f_{\mathrm{HC}} = 45.2$ Hz.

III. Fabrication of the Actuator Components

A. Fabrication of the Coil

As mentioned in Section II-A, the bobbin was manufactured with industrial nylon (polyamide 6), due to its low cost and also because it has a tensile strength of 78 N/mm^2 and a low coefficient of friction. A schematic of the bobbin design is shown in Fig. 8. The thickness of the bobbin ends and the central tube was minimized to withstand the maximum stresses produced by the interaction between the winding and the magnet.

The winding was performed with a 10 AWG wire of 2.59 mm in diameter according to the design parameters shown in Table I. Its resistance ($R_{\mathrm{Coil}}^{\mathrm{exp}}$) was measured using a multimeter HP 34401A and a current source HP 6268B (30 A), obtaining a value of (25.9 ± 0.1) mΩ. Likewise, its impedance Z_{Coil} was experimentally characterized as a function of the frequency using an load ratio control meter Agilent E4980A, in the range between 20 Hz and 2 MHz. In particular, the value of the inductance $L_{\mathrm{Coil}} = (87 \pm 1)$ μH of the manufactured winding was obtained using a characteristic frequency of $\sim$50 Hz, calculated from the theoretical time constant $\tau_{\mathrm{Coil}}^{10\ \mathrm{AWG}}$. The parameter values obtained for the fabricated coil match the computed ones within a 4% tolerance.

TABLE I

Computed Optimal Design Parameters of a Multilayer Winding Magnetic Actuator Based on 10 AWG Copper Wire With a Driving Voltage of 10 V and a Magnet Remanence of 1.02 T. A SF40% Was Used to Design the Experimental Device. The Values Marked With an Asterisk Were Measured Directly in the Manufactured Coil, While the Rest Were Calculated

	Computed (SF100)	Computed (SF40)	Fabricated
Magnet ratio α	5.33	5.33	5.33
Coil ratio β	2.59	2.59	*2.6
Wire diameter d_w [mm]	2.588	2.588	2.588
Wire length l_w [m]	4.16	7.54	7.97
Coil length l_C [mm]	29.8	29.8	*30.5
Coil inner radius r_C [mm]	11.5	11.5	*11.5
Coil thickness $R_C - r_C$ [mm]	9.3	14.4	*14.8
Magnet radius R_m [mm]	7.5	7.5	7.5
Magnet length L_m [mm]	40	40	40
Coil resistance R_{Coil}^{min} [mΩ]	13.4	24.5	*25.9
Coil inductance L_{Coil} [μH]	30.2	86.3	*87
Coil time constant τ_{Coil} [ms]	2.25	3.52	3.55
Max. Current (1 s) I_C^{max} [A]	745	408	386
Max. Pulse Energy E_p^{max} [kJ]	7.45	4.08	3.86
Peak force per amp $\lvert\vec{f}_C^{max}\rvert$ [$\frac{\mathrm{N}}{\mathrm{A}}$]	0.187	0.254	0.251
Total peak force $\lvert\vec{F}_C\rvert$ [N]	139.8	103.6	96.9

B. Fabrication of the Actuator Nucleus

The coil nucleus was given by a cylindrical rod containing a NeFeB magnet fixed inside. Ideally, this rod should be made of a non-magnetic, non-conductive, light, and rigid material. A relative magnetic permeability close to 1 would avoid a distortion of the modeled field during the optimization process, and in turn, a magnetization of the rod that would not only decrease the efficiency of the device, but also make it lose its linearity. The low conductivity of the material would reduce the energy loss due to eddy currents [16]. Finally, the low density and the rigidity of the rod are necessary to reduce its inertia and avoid a deformation of the nucleus in the presence of both traction and compression forces (considering the reduced size of the gap r_g).

Taking into account the aforementioned considerations, two types of the magnetic nucleus were manufactured. The first was made of 304 L stainless steel (relative magnetic permeability $\mu_{304L} = 1.008$) and had a longitudinal groove pattern on the rod to avoid the induction of eddy currents in the angular direction. An illustrative diagram of the design of the steel rod is presented in Fig. 9(a), where the sections colored in light blue represent solid steel cylinders with grooves 2 mm wide and 7 mm deep arranged every 90° (black lines). The centerpiece (uncolored) consisted of a steel tube with 2 mm wall thickness containing the magnet. The total weight of the rod (including the magnet) was 238 g [see Fig. 9(b)].

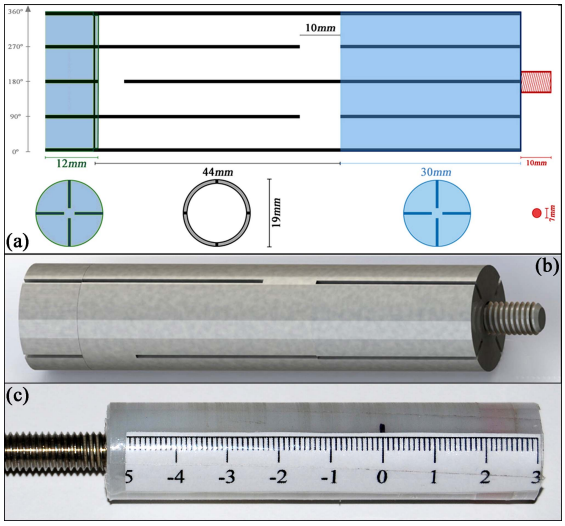

Fig. 9. Magnetic actuator nucleus. (a) Schematic of the steel nucleus design. The groove pattern reduces the energy loss due to the induction of eddy currents. (b) CAD representation of the steel nucleus. The fabricated piece was made from a 2 mm thick 304 L steel tube containing the NeFeB magnet. (c) Photograph of the nylon nucleus.

This hard nucleus was specifically designed for the magnetic piston described in [8] and [9]. The second nucleus, shown in Fig. 9(c), was made of the same type of nylon used in the bobbin and had a weight of 84 g with the magnet inside.

The magnets inserted in each rod were chosen according to the geometrical ratio $\alpha = 5.33$, having a radius of 7.5 mm, a remanent magnetization of $B_r = (1.02 \pm 0.01)$ T, and a coercivity of ∼950 kA/m at 293K.

IV. Characterization of the Magnetic Actuator

In this section, we analyze the performance of the magnetic actuator by characterizing the magnetic field and the tensile force exerted by the device for different displacements (z) and amplitudes of the current pulse (I_C). The experimental results are compared with the numerical model calculations. At the end of this section, the response time of the system is analyzed and thermal aspects of both the actuator and the control module described in the Appendix are also discussed.

A. Force $|\vec{F}_C|$ and Magnetic Field $|\vec{B}_C|$ Versus. Displacement z

First, we searched for the optimal displacement point z_{op}, defined as the distance between the centers of the coil and the magnet for which the force $|\vec{F}_C|$ is maximized. A photograph of the experimental setup employed for this purpose is shown in Fig. 10. To avoid distortions of the magnetic field, the coil was fixed to a rigid wooden plate. The actuator nucleus was fixed to a "S" type load cell BSL MTS-1 used to take static measurements of $|\vec{F}_C|$. In order to carry out this measurement, a rule graduated in millimeter was added to the tube that constitutes the nucleus of the actuator and z was determined by taking high-resolution photographs of the insertion plane of the rod into the coil. The coil was powered with 28 A dc pulses with a duration of ∼3 s for each position. The absence

Fig. 10. Setup used to characterize the pull/push actuator strength for different displacements and current amplitudes. The coil was fixed to a rigid wooden platform, while the load cell was fixed to an optical table.

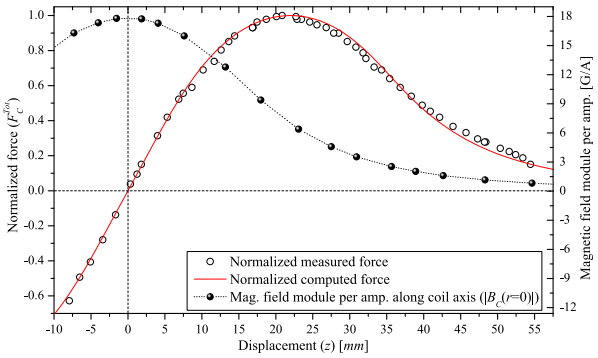

Fig. 11. Magnetic field strength (right axis) and force developed by the actuator $|\vec{F}_C|$ (left axis) as a function of the displacement z. Circles: measured data. Red solid line: corresponds to the numerical simulation shown in Fig. 4, computed for parameters of the manufactured coil ($\beta = 2.6$; $R_{\text{Coil}}^{\text{exp}} = 25.9$ mΩ). Both the experimental and simulated curves were normalized using their maximum value.

of interference of the electromagnetic pulse in the reading of the force sensor was verified. The experimental results were compared with a numerical simulation performed by setting the parameters of the manufactured coil (see Table I) in the code described in [1]. Fig. 11 shows an excellent agreement between the displacement curve obtained from the experiment and the calculated one. The optimal displacement value was $z_{\text{op}} = 22$ mm for both nuclei. In addition, Fig. 11 shows the magnitude of the magnetic field of the coil $|\vec{B}_C|$ measured as a function of z by means of a Gaussmeter F.W. Bell 4048. The linearity of $|\vec{B}_C|$ with I_C was also verified finding a ratio of 17.8 G/A. The distance between the maximum of $|\vec{F}_C|$ and $|\vec{B}_C|$ corresponds to the separation between the center of the coil and the center of the magnet.

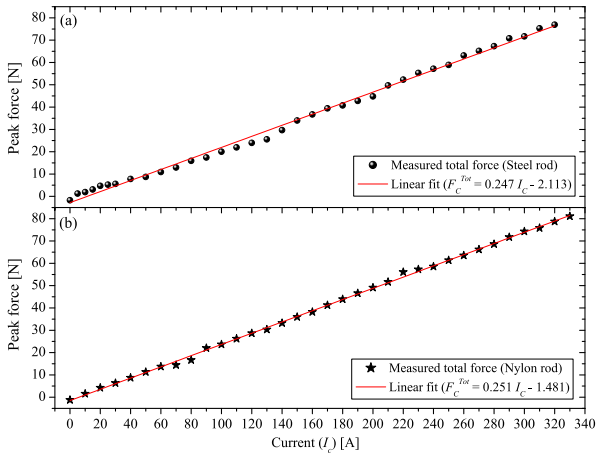

Fig. 12. Force developed by the fabricated actuator $|\vec{F}_C|$ versus current I_C for a case with $z_{\text{op}} = 22$ mm. The data were fitted according to a linear model where the slope of the line represents the parameter $|\vec{f}_C^{\max}|$. The error in these measurements is 2 A in I_C and 2 N in $|\vec{F}_C|$. (a) Measurements taken with the steel rod. Here, $|\vec{f}_C^{\max}| = (0.247 \pm 0.003)$ N/A. (b) Measurements taken with the nylon rod. In this case, $|\vec{f}_C^{\max}| = (0.251 \pm 0.002)$ N/A.

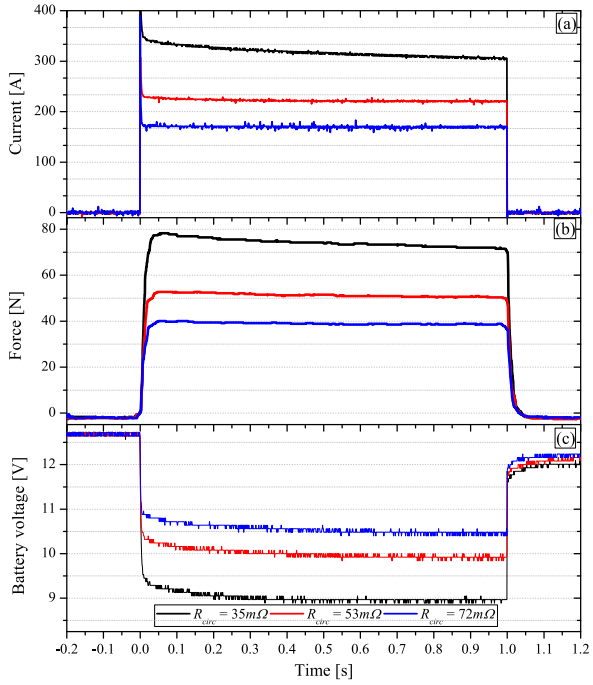

Fig. 13. Current I_C, force $|\vec{F}_C|$, and battery voltage as a function of time for a case with $z_{\text{op}} = 22$ mm and $t_p = 1$ s set in the magnetic actuator using the steel magnetic nucleus. Measurements were made for three resistance values of the circuit R_{circ}, where $R_{\text{circ}} = 35$ mΩ was the lowest possible. The stability of the system (evaluated through the variation of the force) for this configuration is within the 6%. (a) Current I_C versus time. This was calculated from the voltage drop in the winding using a temperature changing value of R_{Coil}. (b) Force exerted by the actuator versus time. (c) Observed decay in the force magnitude is correlated with resistance change due to the coil heating and the decay in the battery voltage.

B. Total Peak Force $|\vec{F}_C|$ Versus Applied Current I_C

The total peak force $|\vec{F}_C|$, i.e., the force measured by adjusting the displacement of the core in z_{op}, was characterized as a function of the current I_C using a regulated power source Rafe (400 A and 30 V) in a range from 0 to 340 A for both nuclei. In these measurements, the control of the magnetic actuator was carried out using the electronics described in the Appendix together with an Arduino UNO programmed with a tailored code to work as a delay/pulse generator (i.e., the trigger signal).

The signal from the force sensor and the voltage drop in the coil (V_C) were acquired using an oscilloscope HP54615B (500 MHz, 1 GSa/s). The current values were computed from V_C and the resistance R_{Coil} by using Ohm's law. In order to obtain the exact values of I_C, these were corrected taking into account the thermal variation of R_{Coil} calculated by means of (4). The temporal evolution of I_C after the actuator activation indicated that this type of supply is not adequate to achieve a stable response of the actuator in pulsed operation, since it has a transient of ∼0.5 s characterized by an overshoot and subsequent oscillations until reaching a continuous level. The calibration curves obtained from the steady part of the current traces are presented in Fig. 12, where a linear relationship between $|\vec{F}_C|$ and I_C can be observed.

The slope of each line represents the force per ampere $|\vec{f}_C^{\max}|$. This parameter took a value of (0.247±0.003) N/A for the measurement using the steel nucleus and (0.251 ± 0.002) N/A for the case using the nylon nucleus. The theoretical estimation for $|\vec{f}_C^{\max}|$ computed from the fabricated coil parameter values (shown in Table I) was 0.251 N/A, then the agreement between the numerical model and the experiments is excellent.

C. Actuator Characterization for Pulsed Operation

As discussed in Section IV-B, the long response times commonly found in high-power current sources make them inadequate for a high-performance pulsed operated magnetic actuator. In practice, a high-current pulse can be generated in a simple and cheap way by using a standard car battery, due to its high capacity and discharge speed. Accordingly, a battery Bosch S455D (CA = 620 A, 55 Ah, and 12.6 V in vacuum) with a measured internal resistance of $R_{\text{Bat}} \approx 8$ mΩ was used.

The actuator performance for pulsed operation using the battery as power source was evaluated by pulse stability, response time, and maximum reachable force, being this limited by the resistance of the circuit formed by the winding and the control module (R_{circ}) described in the Appendix. An example of the curves obtained for three values of R_{circ}, setting the steel nucleus displacement in $z_{\text{op}} = 22$ mm, is shown in Fig. 13. The minimum possible resistance value for this circuit was $R_{\text{circ}} = 35$ mΩ. Measurements of the current I_C, the force $|\vec{F}_C|$, and the voltage at the terminals of the battery were carried out with pulses of 1 s of duration.

Fig. 13(a) shows the current pulse I_C calculated from the voltage drop in the winding and the value of its resistance (variable with temperature). It is worth noting that the pulse shape is remarkably close to a square pulse, with a slight difference given by the peak that takes place when the actuator is activated. The force exerted by the actuator is plotted in Fig. 13(b). A smoothing filter was applied to remove high-frequency noise from the measured data. It can be seen that for low values of R_{circ} (i.e., higher currents), the resistance

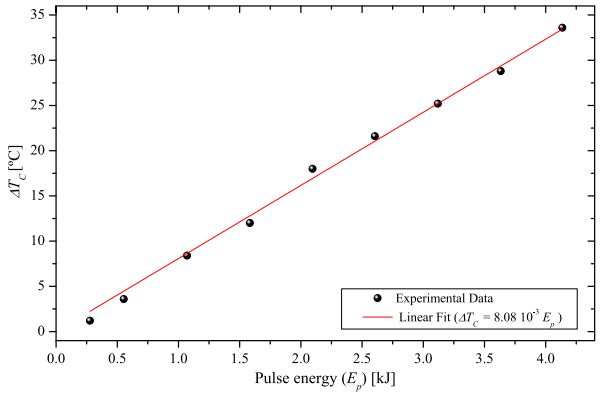

Fig. 14. Thermal variation of the coil versus pulse energy E_p. The linear fit of the experimental results can be used to estimate the coil heating under different durations, amplitude, and shape of the current pulses.

variation due to wire heating becomes increasingly noticeable. The percentage variation of the force observed in each case correlates perfectly with the change in R_{Coil} calculated with (4). The measured forces were compared with those calculated using the calibration line in Fig. 12, finding a good agreement in every case. Finally, Fig. 13(c) shows the voltage at the battery terminals as a function of time. Considering the internal resistance of the battery, the voltage drops in each case are within the estimates at the design stages presented in Section II.

The response time of the actuator (T_r^{exp}), i.e., the minimum time needed for the system to reach 90% of the maximum force after activation, was obtained by decreasing the duration of the pulse t_p to the limit value at which the measured force did not reach equilibrium. From this analysis, a T_r^{exp} between 6 and 10 ms was found (depending on the current amplitude), and these values result very similar to the estimation carried out in Section II-D.

D. Thermal Characterization

As discussed in Section II-A, the system was designed considering different thermal aspects that determine the performance of the actuator and constitute the main causes of failure. Consequently, the thermal response of the actuator was characterized in order to experimentally estimate the limits of its main control parameters (i.e., I_C and t_p). The temperature distribution in the winding was computed for the stationary case [14] using the optimal R_C/r_C ratio in order to determine the best position to insert a temperature sensor inside the coil. The latter was given by a K-type thermocouple, connected to a Fluke: 2190A analog thermometer and an Arduino UNO board employed to take measurements in real time.

Initially, the temperature variation of the coil ΔT_C was measured by applying rectangular current pulses of different duration t_p. Likewise, the temperature variation in the winding was analyzed for different current magnitudes. A general representation of this variation, independent of the shape, and duration of the pulse, is obtained by plotting ΔT_C as a function of the supplied energy E_p. The results, presented in Fig. 14, show a linear relationship between ΔT_C and E_p in the energy range under study.

Finally, the thermal decay time of the winding was studied for different durations of the activation pulse and a fixed current of 250 A. The results show that this time ranges from a few minutes to even hours, depending on the duration and intensity of the pulse. In order to reduce the recovery time of the actuator, a cooling system was implemented by locating two personal computer (PC) coolers diametrically opposite to the coil axis. This simple cooling system made it possible to reduce the waiting time between executions of the actuator by 60%. More complex and effective cooling strategies can be implemented [21], nevertheless, the heat generated by the Joule effect during the current pulse is far greater than the thermal power that can be extracted by a standard refrigeration system (e.g., external heat exchanger or forced convection), so its implementation would not mean an improvement in the maximum energy that can be delivered to the actuator in the pulsed regime. Such an improvement would be possible by implementing a cooling method that allows to modify the initial winding temperature T_i.

V. Conclusion

In this paper, a strategy for the design of a sleeve permanent magnet actuator optimized to maximize the pulling/pushing force was presented. The design was based on the calculation of the limiting current allowable in the coil determined by the Joule heating, and considering thermal and mechanical aspects of the construction materials involved. Moreover, the winding geometry was optimized by means of the electromagnetic numerical model detailed in [1] and [7].

The first-principle thermal model described, here, was implemented by setting an initial winding temperature of 20 °C and a maximum of 55 °C, nevertheless, calculations can be carried out for another temperature interval, for example, to improve the device performance by using a cooling system to achieve a lower T_i, or replacing the fabrication materials to increase T_f. Furthermore, the optimization procedure can be performed for a pulse with an arbitrary geometry and temporal evolution, or also extended it to another conducting materials or magnet types. In addition, the calculations can be reformulated for a continuous driving signal where the heat dissipation to the air and the nucleus, or the effect of the resistance inhomogeneity in the winding, could be considered.

In Section II-C, its been proven that the values of $R_{\text{Coil}}^{\min}$ and $I_C^{\max}$ obtained from the thermal analysis in Section II-A, actually maximize the total peak force ($|\vec{F}_C|$) generated by the actuator, being this a crucial point of the work.

The fabricated device was characterized for pulsed operation using two types of power sources, observing that a standard car battery was suitable to generate low-noise, high-power rectangular current pulses providing good performance stability. However, this source has the disadvantage of requiring an additional high-power resistance to regulate the amplitude of the pulses and must be recharged or replaced after several executions of the device.

The linearity of the actuator, and the agreement between the experimental results and theoretical calculations was excellent for the two types of magnetic nucleus employed. The numerical model was able to reproduce the experiments, not only

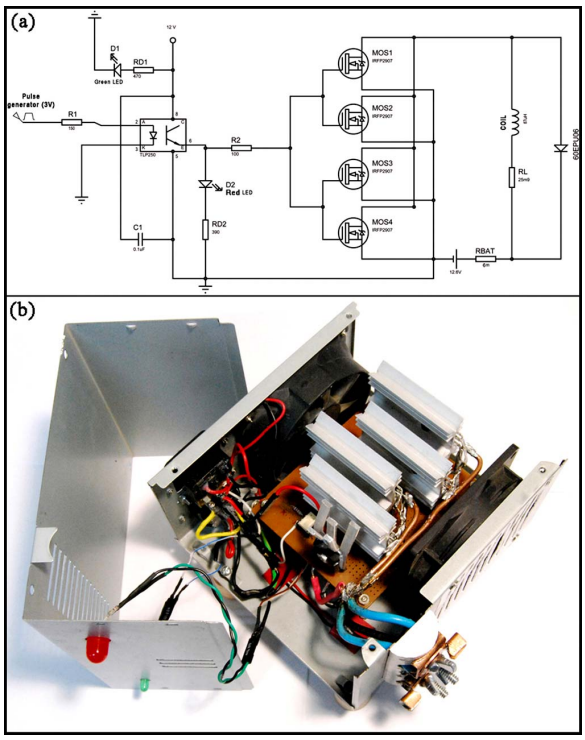

Fig. 15. Control circuit of the magnetic actuator. (a) Circuit schematic. (b) Photograph of the device.

in the actuator peak force, but also in its spatial distribution along the coil axis.

This design protocol can be used to optimize other relevant parameters besides the force (such as the stroke length, the coil bandwidth, the performance stability, and so on) and generalized to other wire diameters, winding or bobbin materials, and magnet types.

Appendix
Actuator Control Circuit

The circuit used to generate the current pulses was an electronic power switch commanded through a digital signal (TTL or CMOS) that activates the conduction of four MOSFET power transistors. This circuit was connected in series with the battery of 12 V_{CC} and the winding of the magnetic actuator as described in the circuit diagram presented in Fig. 15(a). The maximum values of voltage and current supported by each MOSFET IRFP2907 were $V_{DSS} = 75$ V and $I_D = 209$ A for continuous current (cc) and $I_D = 840$ A for pulsed operation.

Considering the high values of current and power required by the magnetic actuator (360 A, ~3600 W), the control unit was designed to withstand the specific thermal loads of this application. Taking into account the internal resistance of the MOSFET IRFP2907 (3.6 mΩ) and the maximum current that each component supports (120 A), it was necessary to use four MOSFETs cooled by aluminum heat sinks and PC coolers. The total resistance of the circuit was 1.6 mΩ. A photograph of the constructed circuit is shown in Fig. 15(b).

The required thermal resistance of the heat sinks was calculated using the "Thermal Ohm Law" [17], obtaining the following balance equation for the stationary case:

$$T_j = P_{\text{dm}} R_{\text{th}(j-a)} + T_a \quad (14)$$

$$R_{\text{th}(j-a)} = R_{\text{th}(j-\text{cap})} + R_{\text{th}(\text{cap}-d)} + R_{\text{th}(d-a)} \quad (15)$$

where T_j is the temperature of the joint, T_a is the room temperature, P_{dm} represents the average power dissipated, $R_{\text{th}(j-\text{cap})}$ is the thermal resistance between the joint and the capsule, $R_{\text{th}(\text{cap}-d)}$ is the thermal resistance between the capsule and the body of the heat sink, and $R_{\text{th}(d-a)}$ is the thermal resistance between the heat sink and the surrounding medium.

In particular, for the employed MOSFET IRFP2907, we have $R_{\text{th}(j-a)} = 40$ °C/W and $R_{\text{th}(\text{cap}-d)} = 0.5$ °C/W. Establishing a peak temperature of 125 °C, the thermal resistance of the MOSFETs should be 3.3 °C/W. Therefore, aluminum heat sinks where employed with a resistance of $R_{\text{th}(\text{cap}-d)} \approx 1.8$ °C/W under forced convection. This stationary analysis is valid when the duration of the pulse is greater than 500 ms, regardless of the duty cycle. The power dissipated in the return diode 60EPU06 was calculated using a transient impedance $Z_{\text{th}(j-\text{cap})} = 0.025$ °C/W [18] since current flows through this component for a time close to RL.

Acknowledgment

The authors would like to thank W. Robertson, B. Cazzolato, and A. Zander for letting others use their code for computing the interaction forces between a permanent magnet and a coil. They also thank J. C. Eggenschwiler for his contribution in the actuator manufacturing. This work was supported by scholarships through CONICET. The materials and equipment were provided by CNEA. The work of J. M. Rosselló and F. E. Giana was supported by the Consejo Nacional de Investigaciones Científicas y Técnicas.

References

[1] W. Robertson, B. Cazzolato, and A. Zander, "Axial force between a thick coil and a cylindrical permanent magnet: Optimizing the geometry of an electromagnetic actuator," *IEEE Trans. Magn.*, vol. 48, no. 9, pp. 2479–2487, Sep. 2012.

[2] S. T. Smith and D. G. Chetwynd, "An optimized magnet-coil force actuator and its application to precision elastic mechanisms," *Proc. Inst. Mech. Eng. C, J. Mech. Eng. Sci.*, vol. 204, no. 4, pp. 243–253, Jul. 1990.

[3] L. Bertini, P. Neri, and C. Santus, "Design and optimization of a compact high-frequency electromagnetic shaker," in *Proc. 11th Int. Conf. Eng. Vib.*, Sep. 2015, pp. 1–9.

[4] R. Kratz and P. Wyder, *Principles of Pulsed Magnet Design*, 1st ed. Berlin, Germany: Springer, 2002.

[5] S. I. Babic and C. Akyel, "Magnetic force calculation between thin coaxial circular coils in air," *IEEE Trans. Magn.*, vol. 44, no. 4, pp. 445–452, Apr. 2008.

[6] R. Ravaud, G. Lemarquand, S. Babic, V. Lemarquand, and C. Akyel, "Cylindrical magnets and coils: Fields, forces, and inductances," *IEEE Trans. Magn.*, vol. 46, no. 9, pp. 3585–3590, Sep. 2010.

[7] W. Robertson, B. Cazzolato, and A. Zander, "A simplified force equation for coaxial cylindrical magnets and thin coils," *IEEE Trans. Magn.*, vol. 47, no. 8, pp. 2045–2049, Aug. 2011.

[8] J. M. Rosselló, "Frontera de estabilidad en sonoluminiscencia y concentración de energía en cavitación transitoria forzada," Ph.D. dissertation, Lab. Cavitación y Biotecnol., Balseiro Inst., Bariloche, Argentina, Mar. 2015.

[9] J. M. Rosselló, R. Urteaga, and F. J. Bonetto, "A novel water hammer device designed to produce controlled bubble collapses," *Exp. Therm. Fluid Sci.*, vol. 92, pp. 46–55, Apr. 2018.

[10] R. A. Matula, "Electrical resistivity of copper, gold, palladium, and silver," *J. Phys. Chem. Ref. Data*, vol. 8, no. 4, pp. 1147–1298, 1979.

[11] M. R. Ward, *Electrical Engineering Science*, 1st ed. New York, NY, USA: McGraw-Hill, 1971.

[12] C. Kittel, *Introduction to Solid State Physics*, 8th ed. New York, NY, USA: Wiley, 2004.

[13] H. W. Sams, *Handbook of Electronics Tables and Formulas*, 6th ed. Indianapolis, IN, USA, Howard W. Sams & Co., 1986.
[14] T. L. Bergman, A. S. Lavine, F. P. Incropera, and P. Dewitt, *Fundamentals of Heat Transfer*, 7th ed. New York, NY, USA: Wiley, 2011.
[15] F. Lanoford-Smith, *Radiotron Designer's Handbook*, 4th ed. Sydney, NSW, Australia: Amalgamated Wireless Valve Co., 1953.
[16] J. D. Jackson, *Classical Electrodynamics*, 3rd ed. Hoboken, NJ, USA: Wiley, 1999.
[17] N. Mohan, T. M. Undeland, and W. P. Robbins, *Power Electronics: Converters, Applications, and Design*, 1st ed. New York, NY, USA: McGraw-Hill, 2009.
[18] B. J. Baliga, *Power Semiconductor Devices*, 1st ed. Boston, MA, USA: PWS Publishing Company, 1996.
[19] M.-D. Calin and E. Helerea, "Temperature influence on magnetic characteristics of NdFeB permanent magnets," in *Proc. 7th Int. Symp. Adv. Topics Elect. Eng. (ATEE)*, Bucharest, Romania, May 2011, pp. 1–6.
[20] Y. Men, J. Rieger, and K. Hong, "Critical strains in tensile deformed polyamide 6 and 6/66 copolymer," *J. Polym. Sci. B, Polym. Phys.*, vol. 43, no. 1, pp. 87–96, 2005.
[21] B. P. Ruddy and I. W. Hunter, "Design and optimization strategies for muscle-like direct-drive linear permanent-magnet motors," *Int. J. Robot. Res.*, vol. 30, no. 7, pp. 834–845, 2011.